Unified lattice Boltzmann method for flow in multiscale porous media

Qinjun Kang
Los Alamos National Laboratory, Los Alamos, New Mexico 87545
and The Johns Hopkins University, Baltimore, Maryland 21218

Dongxiao Zhang
Los Alamos National Laboratory, Los Alamos, New Mexico 87545

Shiyi Chen
The Johns Hopkins University, Baltimore, Maryland 21218
and Peking University, Beijing, China

(Received 30 July 2002; published 21 November 2002)

In this paper, we develop a unified lattice Boltzmann method for flow in multiscale porous media. This model not only can simulate flow in porous systems of various length scales but also can simulate flow in porous systems where multiple length scales coexist. Simulations of unidirectional steady flow through homogeneous and heterogeneous porous media both recover Darcy's law when the effects of inertial forces and Brinkman correction may be negligible. Direct use of this model on the usual computational nodes, with zero resistance on void spaces and infinite resistance on solid walls, gives results that agree well with analytical solutions. Simulations performed on a fractured porous system show that the method presented here gives very good overall permeability values for the whole fractured system. A series of simulations is performed on a simplified fractured system. The results indicate that, when the ratio of the permeability of the rock matrix to the fracture permeability calculated by the cubic law is less than 10^{-4}, the effects of the rock matrix flow are negligible, and the discrete-fracture models that ignore such flow are plausible. When the ratio is larger than 10^{-4}, the matrix flow has significant effects on the fractured system, and the assumption that the matrix is impermeable does not hold. Therefore, the use of the cubic law to calculate the fracture permeability may cause a significant error. It is also indicated that the larger the ratio of the width of the porous matrix to that of the fracture, the more significant is the error caused by using the cubic law.

DOI: 10.1103/PhysRevE.66.056307 PACS number(s): 47.55.Mh

I. INTRODUCTION

Flow and transport in porous media are usually observed physically and treated theoretically at various scales: at microscopic (pore), macroscopic (laboratory, local), and field-scales. Dominant processes and governing equations may vary with the scale. In many situations of flow in porous media, two or multiple scales coexist and are of more or less equal importance. One such example is flow in fractured porous systems. Flow and solute transport in naturally fractured porous media have attracted attention due to their importance in water resources, pollution migration in aquifers, and radioactive waste reposition [1,2]. Owing to the statistically complex distribution of geological heterogeneity and the multiple length and time scales, three approaches [3,4] are commonly used in describing fluid flow and solute transport in naturally fractured porous formations: (1) discrete-fracture models, (2) continuum models using effective properties for discrete grids, and (3) hybrid models that combine the above two.

The discrete-fracture models are based on the observation that the permeability of a fracture is usually much larger than that of the rock matrix. As a result, most of the flow is through the fracture network as long as the fractures are well connected, meaning that the connectivities as well as the distributions of the fractures determine the flow pattern in the fractured formation. With this fact in mind, the discrete-fracture models only account for the flow through the fractures [5–8], assuming the matrix to be impervious. Although these models can realistically describe the distribution of fractures and the flow and mass transfer between fractures and matrix, they can only be applied to a small-scale study because of their complexity and the limitations of the numerical methods involved.

A typical continuum model includes a limited number of regions in which physical properties are uniform. The physical properties computed from a fracture network with an impervious matrix are volume averaged for the total rock size, which includes fractures and matrix [9,10]. Part of the primary input data into these continuum models [11,12] is the permeability of the fracture system assigned to the various regions of the models. The continuum models can be applied to very large-scale studies. However, they can easily miss locally dominant phenomena, such as mass and momentum transfer by primary fractures.

Hybrid models are a combination of discrete-fracture and continuum models in which the large-scale dominant fractures are represented discretely and small fractures are modeled through a network block [13]. Wen *et al.* [14] modeled deterministically fractured zones and used a stochastic con-

tinuum model for nonfractured areas. Lee *et al.* [4] developed a hierarchical approach to model flow in a naturally fractured reservoir with multiple length scale fractures. The permeability contribution from short fractures is derived in an analytical expression and used as an enhanced matrix permeability for the next-scale (medium-length) calculation. The effective matrix permeability associated with medium-length fractures is numerically solved by using a boundary element method. The long fractures are modeled explicitly as major fluid conduits.

This study develops a unified method applicable to various length scale systems as well as to systems where multiple length scales coexist. The length of the scales in this method can be as small as pore scales (on the order of micrometers), as large as field scales (on the order of meters to kilometers), or a mixture of various scales, depending on the porous formations under consideration. This method is based on the lattice Boltzmann (LB), a numerical method based on microscopic models and mesoscopic kinetic equations. This feature gives the LB method the advantage of studying nonequilibrium dynamics, especially in fluid-flow applications involving interfacial dynamics and complex boundaries (geometries). Since its appearance, the LB method has proved to be competitive in studying a variety of flow and transport phenomena (see [15–19] for reviews), including single- or multiphase flow [20–24] and chemical dissolution [25] in porous media. This feature, however, also makes it difficult for the original LB method to be applied to systems with larger length scales.

Previous efforts have been made to develop macroscopic porous media models for lattice gas and LB methods by introducing a resistance force by dynamically altering the local flow velocity; this process provides the necessary momentum sink. This fundamental idea appeared in a rudimentary form in early work on lattice gas automata [26]. More recently, it was applied to the LB method for simulations of flow through porous fiber tows to calculate the overall permeability of a fiber bundle [27]. Freed [28] made some corrections to the above model, to recover flow through a resistance field with arbitrary resistance tensor components. Direct use of this model on the usual computational nodes, with zero resistance on void space and infinite resistance on no-slip sites, will match results from the regular LB method on pore scale. Replacing the usual computational nodes with porous media nodes in the volume supposed to be occupied by a porous medium, however, will extend the applicability of this model to systems with much larger length scales.

The above-mentioned model can be applied to pore-scale systems as well as macroscopic systems. To apply it to systems where multiple length scales coexist, it is advantageous to extend it to nonuniform meshes. Since He and Luo [29] and Abe [30] demonstrated that the LB equation is a discretized form of the continuous Boltzmann equation and that the discretization of physical space is not coupled to the discretization of momentum space, several efforts have been made to treat the curved boundaries and to control the grid density at desirable regions.

Succi *et al.* [31,32] and Xi *et al.* [33] proposed finite-volume LB methods for simulation of fluid flows in complex geometries. He *et al.* [34–36] proposed an interpolation-supplemented LB model to simulate a two-dimensional (2D) channel flow with sudden expansion on a nonuniform mesh and flows past a circular cylinder in a curvilinear coordinate system. Mei and Shyy [37] developed a LB method in a generalized body-fitted coordinate system. Filippova and Hanel [38] developed a second-order-accuracy boundary condition for the LB method to treat a curved boundary on the regular structured mesh. Mei *et al.* [39] improved this scheme and further extended it to three dimensions [40]. Lin and Lai [41] proposed a composite block-structured LB method for the simulation of 2D, incompressible fluid flows. Lee and Lin [42] developed a characteristic Galerkin method for a discrete Boltzmann equation to simulate fluid flows in complex geometries.

In this study, we use the interpolation-supplemented LB model proposed by He *et al.* [34]. Because this model adds only one new interpolation step between the streaming and relaxation steps in the conventional LB method and retains the local property of the two steps, it is easy to apply to the above-mentioned macroscopic porous media model. Extension of the macroscopic porous media model to a nonuniform grid and the intrinsic parallelism of the LB method enable the proposed unified model to simulate flow in large-scale fractured media with the coexistence of various length scales.

II. MODEL AND THEORY

A. Lattice Boltzmann method

Fluid flow can be simulated with the following LB equation:

$$f_i(\mathbf{x}+\mathbf{e}_i\delta_t, t+\delta_t) = f_i(\mathbf{x},t) - \frac{f_i(\mathbf{x},t) - f_i^{eq}(\rho,\mathbf{u},T)}{\tau}, \quad (1)$$

where f_i is the particle velocity distribution function along the i direction, δ_t is the time increment, τ is the relaxation time relating to the kinematic viscosity by $\nu=(\tau-0.5)RT$, and f_i^{eq} is the corresponding equilibrium distribution function, which has the following form:

$$f_i^{eq}(\rho,\mathbf{u},T) = \omega_i\rho\left[1+\frac{\mathbf{e}_i\cdot\mathbf{u}}{RT}+\frac{(\mathbf{e}_i\cdot\mathbf{u})^2}{2(RT)^2}-\frac{\mathbf{u}^2}{2RT}\right], \quad (2)$$

where R is the gas constant, and $\mathbf{u}$, ρ, and T are the velocity, density, and temperature of the fluid, respectively. The $\mathbf{e}_i$'s are the discrete velocities and the ω_i's are the associated weight coefficients. For the 2D, nine-speed LB model, we have $RT=1/3$, and

$$\mathbf{e}_i=\begin{cases} 0, & i=0, \\ \left(\cos\dfrac{(i-1)\pi}{2},\sin\dfrac{(i-1)\pi}{2}\right), & i=1\text{–}4, \\ \sqrt{2}\left(\cos\left[\dfrac{(i-5)\pi}{2}+\dfrac{\pi}{4}\right],\sin\left[\dfrac{(i-5)\pi}{2}+\dfrac{\pi}{4}\right]\right), & i=5\text{–}8. \end{cases} \tag{3}$$

The corresponding weight coefficients are $\omega_0=4/9$, $\omega_i=1/9$ for $i=1,2,3,4$, and $\omega_i=1/36$ for $i=5,6,7,8$. The density and velocity of the fluid are calculated using

$$\rho=\sum_i f_i, \tag{4}$$

$$\rho\mathbf{u}=\sum_i \mathbf{e}_i f_i. \tag{5}$$

It is well known that, using the Chapman-Enskog expansion, the above LB equation, Eq. (1), recovers the correct continuity and momentum equations at the Navier-Stokes level,

$$\frac{\partial\rho}{\partial t}+\boldsymbol{\nabla}\cdot(\rho\mathbf{u})=0, \tag{6}$$

$$\frac{\partial(\rho\mathbf{u})}{\partial t}+\boldsymbol{\nabla}\cdot(\rho\mathbf{u}\mathbf{u})=-\boldsymbol{\nabla}p+\boldsymbol{\nabla}\cdot[\rho\nu(\boldsymbol{\nabla}\mathbf{u}+\mathbf{u}\boldsymbol{\nabla})], \tag{7}$$

where $p=\rho RT$ is the fluid pressure.

B. Macroscopic porous media modeling

Here we adopt the macroscopic porous media model introduced by Freed [28]. It is an improvement on the model of Spaid and Phelan [27], which is based on the general idea that an external force can be introduced into the macroscopic fluid dynamics by altering the local and instantaneous velocity during the collision step. Interphase and gravity forces have been achieved in this fashion [43,44].

Here we give a brief review of the macroscopic porous media model; readers may refer to [28] for more details. Some additional notation is introduced to help describe the method: $\tilde{\mathbf{u}}$ is the precollision (poststreaming) velocity; $\mathbf{u}'$ is the postcollision velocity; $\overline{\mathbf{u}}$ is the ''centered-mean'' velocity, i.e., the resulting mean field continuum velocity; f_i is the precollision (poststreaming) distribution, $\tilde{f}_i\equiv f_i^{eq}(\rho,\tilde{\mathbf{u}},T)$, $f_i'\equiv f_i^{eq}(\rho,\mathbf{u}',T)$, and $\overline{f_i}\equiv f_i^{eq}(\rho,\overline{\mathbf{u}},T)$, where the functional form of f_i^{eq} is given by Eq. (2). The right-hand side (RHS) of Eq. (1) can be defined as the collision operator $\mathcal{C}$, and for the basic LB scheme may be written as

$$\mathcal{C}(f_i)=f_i-\frac{f_i-\tilde{f}_i}{\tau}. \tag{8}$$

By using a new velocity $\mathbf{u}'$ in the equilibrium distribution, the collision operator becomes

$$\mathcal{C}(f_i)=f_i-\frac{f_i-f_i'}{\tau}, \tag{9}$$

and an external force $\mathbf{F}$,

$$\mathbf{F}=\frac{\rho}{\tau}(\mathbf{u}'-\tilde{\mathbf{u}}), \tag{10}$$

is introduced into the mean dynamics and appears on the RHS of Eq. (7) [43]. To treat the porous media region as a ''resistance field'' where the superficial velocity is taken to be an appropriate continuum velocity variable, it is necessary to let

$$\frac{\rho}{\tau}(\mathbf{u}'-\tilde{\mathbf{u}})=-\rho\underline{\underline{R}}\cdot\overline{\mathbf{u}}. \tag{11}$$

The resistance tensor $\underline{\underline{R}}$ is defined as

$$\underline{\underline{R}}=\nu\underline{\underline{k}}^{-1}, \tag{12}$$

where ν is the fluid kinematic viscosity, and $\underline{\underline{k}}$ is a (symmetric) tensor of permeability coefficients. The centered-mean velocity $\overline{\mathbf{u}}$ is defined as [43]

$$\overline{\mathbf{u}}=\tilde{\mathbf{u}}+\frac{\mathbf{F}}{2\rho}=\left(1-\frac{1}{2\tau}\right)\tilde{\mathbf{u}}+\frac{1}{2\tau}\mathbf{u}'. \tag{13}$$

Substituting Eq. (13) into Eq. (11) and solving for $\mathbf{u}'$ gives

$$\mathbf{u}'=\left[\underline{\underline{I}}+\frac{1}{2}\underline{\underline{R}}\right]^{-1}\left[\underline{\underline{I}}-\left(\tau-\frac{1}{2}\right)\underline{\underline{R}}\right]\cdot\tilde{\mathbf{u}}=\underline{\underline{G}}\cdot\tilde{\mathbf{u}}, \tag{14}$$

where $\underline{\underline{G}}$ is the ''velocity adjustment tensor,'' which depends on $\underline{\underline{R}}$ and τ. When the resistance tensor is diagonal, Eq. (14) may be written as

$$u_\alpha'=G_\alpha\tilde{u}_\alpha \tag{15}$$

and the expression for G_α becomes

$$G_\alpha=\frac{1-\left(\tau-\frac{1}{2}\right)R_\alpha}{1+\frac{1}{2}R_\alpha}. \tag{16}$$

Direct use of Eq. (9) for the collision step, in conjunction with Eq. (14), results in an artifact A in the momentum transport equation at the viscous level of the form

$$A=\nabla\cdot(\rho\overline{\mathbf{uu}}-\rho\mathbf{u}'\mathbf{u}'), \tag{17}$$

where A appears on the RHS of the momentum transport equation along with the resistance force $\mathbf{F}=-\rho\underline{\underline{R}}\cdot\overline{\mathbf{u}}$. The artifact can be removed by replacing the equilibrium distribution f_i' used in Eq. (9) by a modified distribution f_i^*,

$$f_i^*=f_i'+\overline{g_i}-g_i', \tag{18}$$

where $\overline{g_i}=g_i(\rho,\overline{\mathbf{u}},T)$, $g_i'=g_i(\rho,\mathbf{u}',T)$, and the function g_i is

$$g_i(\rho,\mathbf{u},T)=\omega_i\rho\left[1+\frac{(\mathbf{e}_i\cdot\mathbf{u})^2}{2(RT)^2}-\frac{\mathbf{u}^2}{2RT}\right]. \tag{19}$$

The complete algorithm for the porous media model may therefore be given as

$$f_i(\mathbf{x}+\mathbf{e}_i\delta_t,t+\delta_t)=f_i(\mathbf{x},t)-\frac{f_i(\mathbf{x},t)-f_i^*(\rho,\mathbf{u},T)}{\tau}, \tag{20}$$

$$f_i^*(\rho,\mathbf{u},T)=\omega_i\rho\left[1+\frac{\mathbf{e}_i\cdot\mathbf{u}'}{RT}+\frac{(\mathbf{e}_i\cdot\overline{\mathbf{u}})^2}{2(RT)^2}-\frac{\overline{\mathbf{u}}^2}{2RT}\right], \tag{21}$$

with $\mathbf{u}'$ and $\overline{\mathbf{u}}$ given by Eqs. (14) and (13). The resulting macroscopic transport equations are

$$\frac{\partial\rho}{\partial t}+\nabla\cdot(\rho\mathbf{u})=0, \tag{22}$$

$$\frac{\partial(\rho\mathbf{u})}{\partial t}+\nabla\cdot(\rho\mathbf{uu})=-\nabla p-\rho\underline{\underline{R}}\cdot\mathbf{u}+\nabla\cdot[\rho\nu(\nabla\mathbf{u}+\mathbf{u}\nabla)], \tag{23}$$

where $\mathbf{u}$ is understood to be the centered-mean velocity $\overline{\mathbf{u}}$, which is the superficial velocity or the flux. It is clear that Eq. (23) recovers Brinkman's equation [45] when the inertial terms on the left-hand side can be neglected. The last term in this equation is called the Brinkman correction, which is usually much smaller than the linear-velocity term for flow through porous media. Hence Eq. (23) is reduced to Darcy's law when flow in porous media is very slow. However, at sites where permeability is very large, i.e., the resistance is very small, the linear-velocity term is negligible compared to other terms and Eq. (23) recovers the Navier-Stokes equation (Brinkman's equation yields Stokes' flow in this case). In the limiting case where the resistance tensor $\underline{\underline{R}}$ is infinite, $\mathbf{u}$ equals zero, which is the no-slip condition at solid walls.

C. Nonuniform grid extension

For simplicity, we only consider a nonuniform, rectangular computational mesh in this study. Following the procedure adopted by He *et al.* [34], let $X_{\alpha,\beta}\equiv(X_\alpha,Y_\beta)$ denote a grid point on an arbitrary rectangular computational mesh in a Cartesian coordinate system, and dX_α and dY_β denote grid sizes,

$$dX_\alpha=X_{\alpha+1}-X_\alpha, \tag{24}$$

$$dY_\beta=Y_{\beta+1}-Y_\beta. \tag{25}$$

The ratios of nonuniform-to-uniform grid sizes are defined as

$$r_x^\alpha=dX_\alpha/\delta_x, \tag{26}$$

$$r_y^\beta=dY_\beta/\delta_y. \tag{27}$$

Given the initial values of f_i at each grid point (X_α,Y_β), the LB system evolves on the nonuniform mesh in the following steps.

(1) Since the precollision value of $f_i(X_{\alpha,\beta},t)$ is known on each grid point (X_α,Y_β), the density ρ and the precollision velocity $\tilde{\mathbf{u}}$, can be calculated from Eqs. (4) and (5) at each grid point. The postcollision velocity $\mathbf{u}'$ and centered-mean velocity $\overline{\mathbf{u}}$ can then be calculated from Eqs. (14) and (13), respectively. The modified equilibrium distribution function can then be constructed using Eq. (21). The postcollision value of $f_i(X_{\alpha,\beta},t)$ is henceforth obtained.

(2) After the collision, advection takes place, and the $f_i(X_{\alpha,\beta}+\mathbf{e}_i\delta_t,t+\delta_t)$ are obtained.

(3) The values of $f_i(X_{\alpha,\beta},t+\delta_t)$ on the mesh grids $X_{\alpha,\beta}$ are computed by interpolation from the values of $f_i(X_{\alpha,\beta}+\mathbf{e}_i\delta_t,t+\delta_t)$ on the points $X_{\alpha,\beta}+\mathbf{e}_i\delta_t$. Then the collision and the advection process are repeated.

D. Discussion of the unified model

In the simulation of flow through a porous system, this model is employed by simply replacing the usual computational nodes with porous media nodes in the region supposed to be occupied by porous medium. Each node in this region is given a permeability value and represents a homogeneous medium with that permeability value. All continuum properties at this node have been volume averaged and satisfy the mass and momentum transport equations given by Eqs. (22) and (23) [28]. At a node in pore space, however, the resistance is specified as zero, all continuum properties are microscopic variables, and Eq. (23) recovers the Navier-Stokes equation. At an impervious wall node where the resistance is given as infinity, the velocity is zero according to Eq. (23), and the nonslip condition is satisfied. This method treats the porous medium nodes, pore nodes, and wall nodes in the same way, although they are at different length scales. Hence, there are no internal boundaries in this model. The extension of this method to a nonuniform grid gives it more flexibility in handling flow in porous systems where multiple length scales coexist.

The unified model presented here is different from other existing multiscale methods. Unlike integrated schemes [46], in which different methods are used to handle individual scales, this unified model uses the same method in regions of different spatial scales and hence avoids the use of complex methods to achieve seamless interfaces between the

different mathematical models at various scales. Compared to the existing multiscale LB schemes [47–49], the unified model eliminates the internal boundaries and can handle a larger scale span because of its utilization of resistance field. On one hand, this model enables us to carefully investigate some regions of great interest while ignoring the flow details in regions far from there. On the other hand, it may not provide such a smooth transition between these regions as do some advanced coarsening techniques like wavelets [50].

Neither the macroscopic porous media model nor its extension to a nonuniform grid changes the feature of parallelism inherent in the basic LB algorithm, which renders the unified model proposed in this paper especially suitable for simulating flow in large-scale fractured media.

III. SIMULATION RESULTS AND DISCUSSION

In the simulations below, the resistance is assumed to be isotropic by setting $R_y = R_x$, so the resistance tensor is purely diagonal. Extending to anisotropic permeability and hence anisotropic resistance fields should be straightforward.

A. Flow in porous media

1. Flow in a homogeneous porous medium

From Eq. (23), Darcy's law should be recovered for steady flow when the inertial and Brinkman correction terms can be neglected. A simple test of unidirectional flow through a homogeneous porous medium is performed to verify the validity of the method described here.

The simulation geometry is a rectangle of size 100×40, based on regular square lattice unit spacings. The permeability value at each node is equal to a constant. At the entrance ($x=0$) and exit ($x=100$), pressure is specified by using the inlet/outlet pressure boundary conditions proposed by Zou and He [51]. At $y=0$ and $y=40$, periodic boundary conditions are applied.

Two types of mesh are used in the simulations: a regular uniform square mesh grid and a uniform rectangular mesh grid. The square mesh grid is 101×41, where the ratios of nonuniform-to-uniform grid sizes are $r_x = r_y = 1$. No interpolation is needed in simulations on this mesh grid. The rectangular mesh grid is 41×21, where $r_x = 2.5$, $r_y = 2$. The quadratic interpolation is used because its accuracy is comparable to the accuracy of the LB method itself.

Figures 1(a), 1(b), and 1(c) show the dependence of the specific discharge on the pressure drop at three values of permeability: 1, 10, and 100, respectively. All quantities are in lattice units. The simulation results on the rectangular mesh agree well with those on the square mesh, indicating the correctness of the interpolation method used in this study; it also confirms that the quadratic interpolation is sufficient for this LB algorithm. The simulation results are in good agreement with analytical solutions based on Darcy's law, especially when the pressure drop is small. At a high pressure drop, the simulation results deviate from the analytical solutions due to inertial effects and the compressibility inherent in the LB method. The simulation results confirm that Eqs. (22) and (23) recover Darcy's law if the flow is steady and the effects of inertial and Brinkman correction terms are negligible.

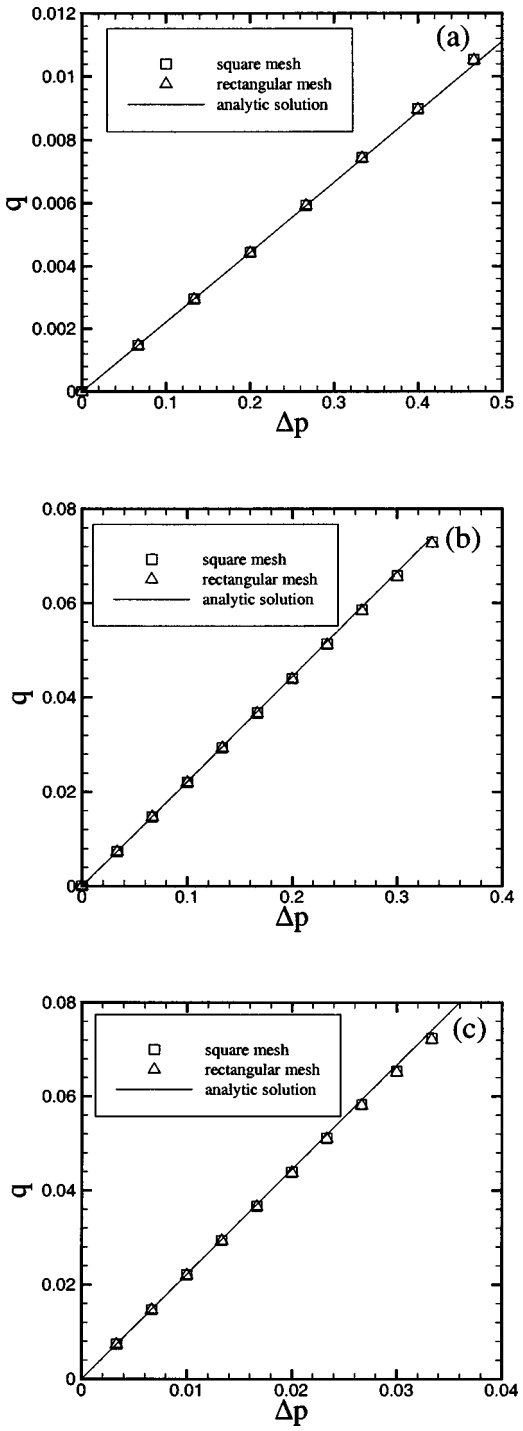

FIG. 1. The dependence of specific discharge on the pressure drop: test of Darcy's law. All quantities are in lattice units. Three values of permeability are used: (a) $k=1$; (b) $k=10$; (c) $k=100$.

2. Flow in a heterogeneous porous medium

We also simulated flows through a bimodal heterogeneous porous medium generated using a two-stage procedure [52]. The field is 16 m $\times$ 16 m, and the grid size is 81×81. The

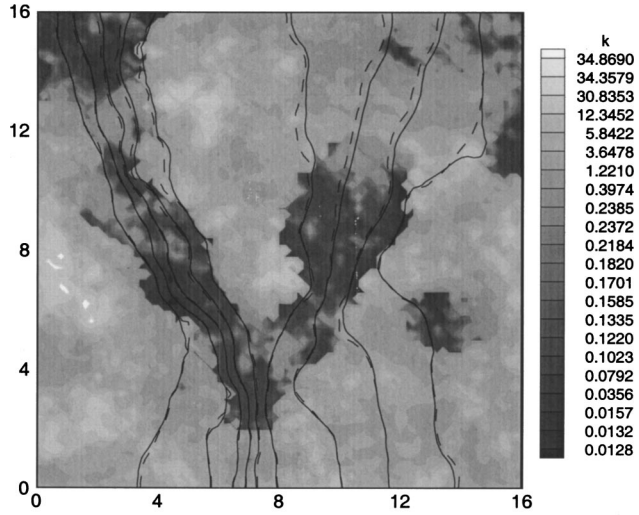

FIG. 2. The permeability distribution and the pressure contours obtained by the current method (solid lines) and FEHM (dashed lines). The field is 16 m×16 m. The pressure (head) is 10.5 m at entrance, and 10 m at exit. The permeability is in units of m^2, and its values are multiplied by 10^{14}. The Reynolds number in the current method is 5.96×10^{-3}.

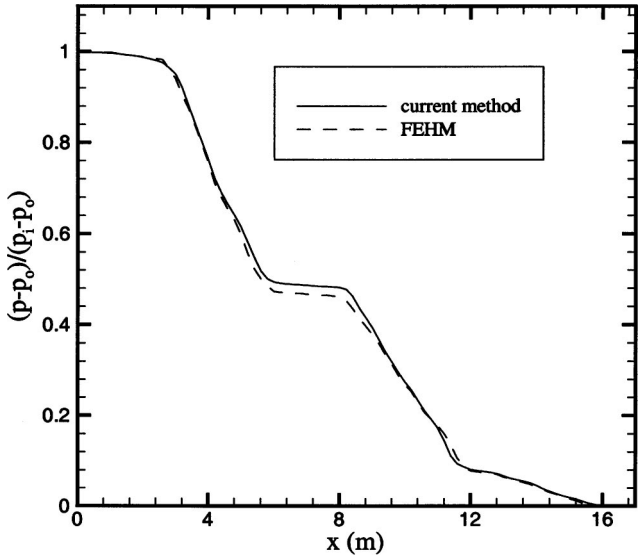

FIG. 3. The dimensionless pressure profile at the centerline ($y=8$ m) obtained by the current method (solid line) and FEHM (dashed line). p_i is the pressure at the entrance, and p_o is the pressure at the exit. The Reynolds number in the current method is 5.96×10^{-3}.

permeability field is composed of two permeability populations: one with a low mean permeability (the black material region), and the other with a high mean value (the white region). The permeability also varies within each region. Overall, the maximum value of the permeability is 6.07×10^{-13} m^2, and the minimum value is 8.46×10^{-17} m^2. The pressure (head) difference between the entrance and the exit is 0.5 m. The density and viscosity of the fluid are 997.81 kg/m^3 and 1.00246×10^{-3} kg m^{-1} s^{-1}.

There is no analytical solution for flow through such a porous medium because of the heterogeneity of the medium, even though the flow is assumed to be steady and Darcy's law is satisfied. To verify the validity of the method in simulating flow through such a medium, we compared our simulation results with those obtained by using the finite-element heat- and mass-transfer code (FEHM) developed by Zyvoloski *et al.* [53]. In both simulations, the grid size is 81×81; pressure (head) is specified at entrance and exit; and velocity along the normal direction of the other two boundaries is set to zero. Notice that in FEHM Darcy's law is used, while in our method Eq. (23) is solved. However, in the case of steady flow with a small Reynolds number, where inertial forces and the Brinkman correction can be neglected, the results of these two methods should be close to each other. The Reynolds number is defined as $\mathrm{Re}=\rho u l/\mu$, where ρ and μ are the density and viscosity of the fluid, respectively, and u and l are the characteristic velocity and length of the system, respectively. Here l is the length of the field, and u is the average horizontal velocity in the whole fluid field.

Figure 2 shows the permeability distribution and the contours of pressure (head) obtained by these two methods. The permeability values are multiplied by 10^{14}. The solid lines are the results obtained with the current method, and the dashed lines are results obtained with FEHM. The Reynolds number in the current method is $\mathrm{Re}=5.96\times10^{-3}$. Apparently, at this Reynolds number, the pressure contours of these two methods agree with each other very well, and they are both mainly distributed in two regions where the permeability values are relatively small. This is correct since in such regions the resistance to the flow is larger and, accordingly, a greater pressure drop is needed to achieve the overall flow rate; hence the pressure contours are denser than elsewhere. Figure 3 shows the dimensionless pressure profile along the horizontal center of the domain (at $y=8$). The results of these two methods are in good agreement.

Figures 4 and 5 show the same quantities as Figs. 2 and 3, but in this case the Reynolds number is $\mathrm{Re}=4.75$. The differences between the results from these two approaches increase with the Reynolds number. At the relatively high Reynolds number of 4.75, the inertial forces become so important that flow is not well represented by Darcy's law.

B. Flow in a 2D channel

In the above section, we tested the validity of the method for flow under situations where the resistance has nonzero finite values. In this section, we test its validity in flow simulations where the resistance is zero or infinite.

The simulation geometry is a rectangle of size 100×24, based on regular square lattice unit spacings. At nodes of $y=0,1,2,22,23,24$, the permeability is set to zero, i.e., resistance is infinite. At other nodes, the permeability is set to infinity, i.e., resistance is zero. At the entrance ($x=0$) and exit ($x=100$), the pressure is specified [51]; at $y=0$ and $y=24$, periodic boundary conditions are applied. This set of permeability values should recover the 2D channel flow between $y=2$ and $y=22$; this flow has an analytical solution. The horizontal velocity has the following form:

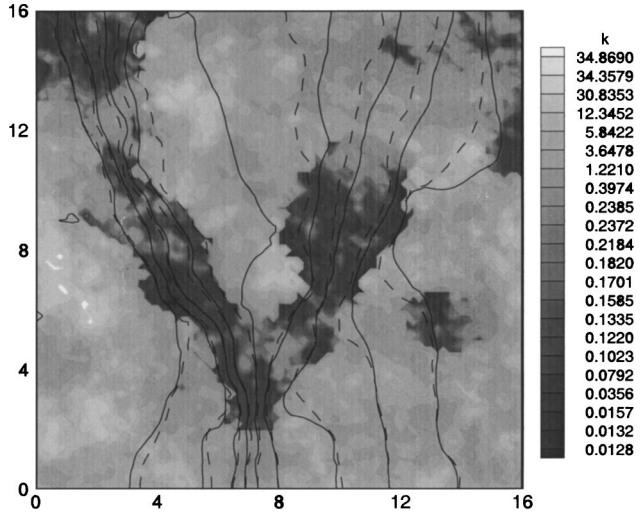

FIG. 4. The permeability distribution and the pressure contours obtained by the current method (solid lines) and FEHM (dashed lines). The field is 16 m×16 m. The pressure (head) is 10.5 m at entrance, and 10 m at exit. The permeability is in units of m^2, and its values are multiplied by 10^{14}. The Reynolds number in the current method is 4.75.

$$u=\frac{h^2\Delta p}{2\mu l}\left[\frac{y-2}{h}-\left(\frac{y-2}{h}\right)^2\right], \tag{28}$$

where h is the channel width, Δp is the pressure drop between the entrance and the exit, μ is the fluid viscosity, and l is the channel length. The averaged velocity is $\bar{u}=h^2\Delta p/12\mu l$, and the permeability can be calculated as

$$k=\frac{\bar{u}\mu l}{\Delta p}=\frac{h^2}{12}. \tag{29}$$

Equation (29) is called the cubic law, and is widely used in discrete-fracture models to calculate the permeability of a single fracture.

Figure 6 shows the horizontal velocity profile normalized by the centerline velocity U_0 of the analytical solution. It is clear that the velocity profile from $y/h=0.1$ to $y/h=1.1$ ($y=2$ to $y=22$) is parabolic; velocity at the nodes out of this region is zero. This is correct because the resistance is infinite at those nodes. It is clear that the 2D channel flow is recovered with excellent accuracy for this setup. The permeability of the channel is also calculated; it is 33.1, very close to the analytical solution obtained from the cubic law (33.3333).

As opposed to the conventional LB method for simulating the 2D channel flow, there are no boundary conditions at $y=2$ and $y=22$. The no-slip conditions at the walls are implemented by prescribing the resistance values there as infinity. This characteristic enables the current method to treat in the same way void spaces, solid walls, and nodes with nonzero finite values of resistance.

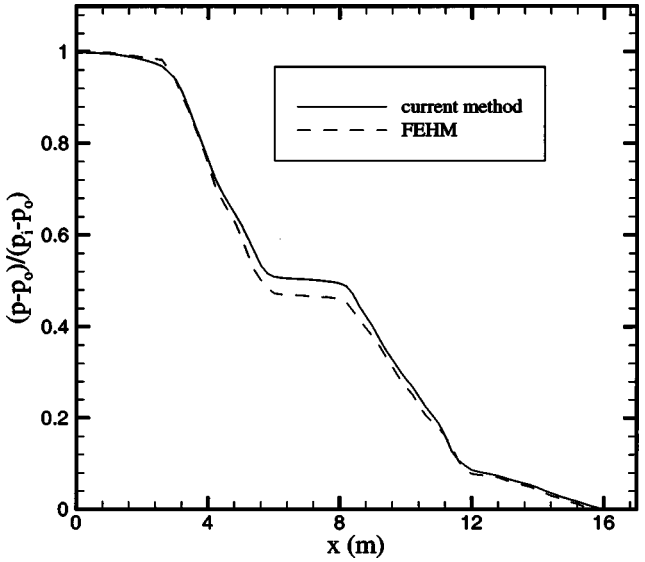

FIG. 5. The dimensionless pressure profile at centerline ($y=8m$) obtained by the current method (solid line) and FEHM (dashed line). p_i is the pressure at the entrance, and p_o is the pressure at the exit. The Reynolds number in the current method is 4.75.

C. Flow through fractured systems

In previous sections, we applied the method presented in this paper to flows in porous media at the field scale and flow in a 2D channel at the pore scale. Now we apply the method to flows in fractured systems where multiple scales coexist. For this purpose, the use of nonuniform grids is advantageous. Figure 7 shows a fractured system constructed by mirroring the original porous medium and leaving a fracture between the original medium and its image. The size of this fractured system is 255×530, and the fracture width is 20, both in lattice units. When the conventional LB method, based on a uniform square grid, is applied to this system, a mesh size of 256×531 is needed. However, if we are interested in only the overall behavior of the fractured system instead of the flow details in the two porous matrices, we may simplify the two porous matrices as homogeneous ones, and use substantially fewer nodes to represent them. Each of the nodes has the permeability value of the original porous medium (0.59 in lattice units, which is used as input at each node). In the simulation with the current method, there is no detailed geometry at the pore scale, and the original porous medium and its mirror are replaced by a homogeneous porous medium. Figure 8 shows the mesh used in the simulation of the current method. The mesh size is only 51×101. r_x is 5.1 at all nodes, and r_y changes smoothly from 1 (inside the fracture) to 12.657 (at $y=0$ and $y=530$). In both simulations, the pressure is specified at the entrance and exit [51], and periodic boundary conditions are applied to the other two boundaries. The permeability in a region is calculated by

$$k=\frac{\bar{u}\mu l}{\Delta p}, \tag{30}$$

where $\bar{u}$ is the average horizontal velocity in this region.

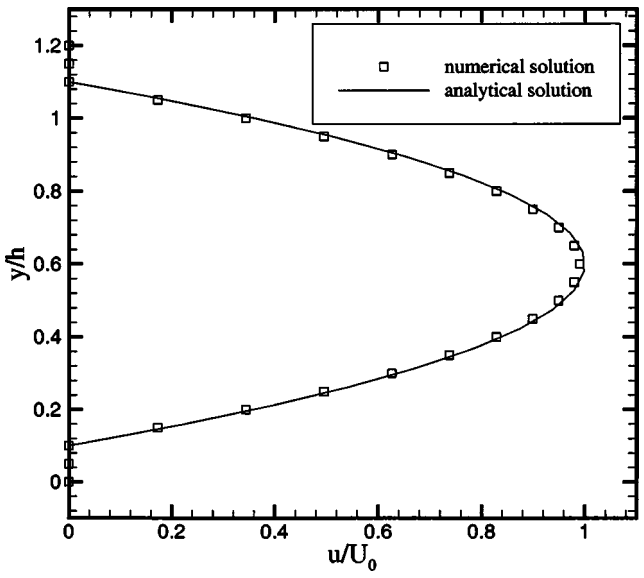

FIG. 6. The horizontal velocity profile (normalized by the centerline velocity U_0 of analytical solution) of 2D channel flow.

Table I shows the permeability values of the bottom half, the top half, the fracture, and the whole system calculated by the conventional LB method and by our current method. It is clear that the permeability values of the porous matrix obtained by the current method are smaller than those calculated by the conventional LB method, and that the permeability value of the fracture obtained by the current method is greater than that obtained by the conventional LB method. This discrepancy is partly due to the heterogeneity of the porous matrix.

As mentioned above, the basis for replacing the usual computational nodes in a region with nodes with uniform permeability values is that the porous matrix in this region is homogeneous. There is no guarantee here that the original porous medium is homogeneous. The local heterogeneity of the medium plays an important role in the interaction between the porous matrix and the fracture and thus has an important effect on the permeability values calculated by Eq. (30) for both the porous matrix and the fracture. However, for the overall permeability of the fractured system, the value obtained in the current method is very close to that obtained by the conventional LB method in spite of the local heterogeneity of the porous matrix. This is very encouraging. For a fractured porous system, we may represent a region of porous medium or minor fractures with considerably fewer nodes having certain permeability values and solve the the flow in this region on a length scale much larger than the pore scale; we should, however, solve flow in a region of major fractures with fine grids. By doing so, we can handle fractured systems where multiple length scales coexist.

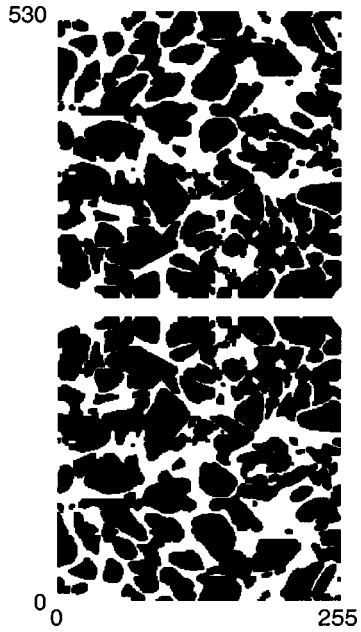

FIG. 7. Geometry of a fractured system. Its size is based on the lattice unit.

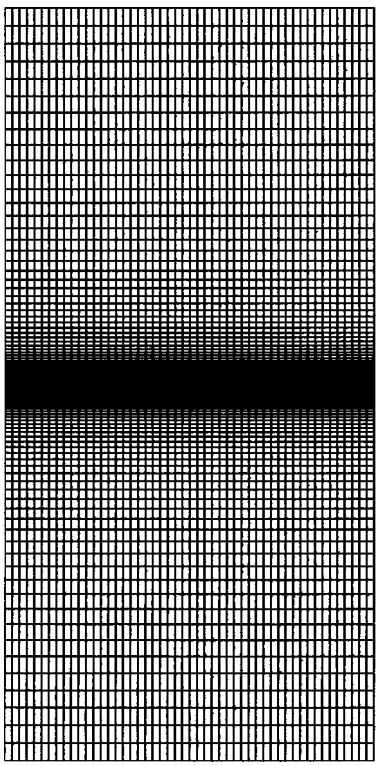

FIG. 8. Nonuniform rectangular mesh used in the simulation of the fractured system.

In the rest of this section, we apply the method presented in this paper to flow via a simplified fractured system to investigate the validity of the cubic law, which is widely used in discrete-fracture models. Figure 9 shows a simplified fractured system, where l is the length along the flow direction, h is the width of the fracture, and h_p is the width of the porous matrix. In our simulations, l is 200 and h is 20, both in lattice units. Two values of h_p (200 and 400) are used. The mesh size in the x direction is 51, with $r_x=4$ at all nodes. In the y direction, the mesh size is 61 in the former case and 101 in the latter case. The value r_y changes smoothly from 1 (inside the fracture) to 9.48 (at $y=0$ and $y=220$ in the former case) and 9.50 (at $y=0$ and $y=420$ in the latter case). Figure 10 shows the mesh used in the simulations on the

TABLE I. Permeability values (in lattice units).

	Top half	Bottom half	Fracture	Overall
Conventional LB	0.64	0.64	35.31	1.94
Current method	0.61	0.61	37.01	1.99
Error	-4.7%	-4.7%	4.8%	2.6%

system with $h_p=200$. Again, the pressure is specified at both ends [51], and periodic boundary conditions are applied at $y=0$ and $y=h_p+h$.

Figure 11 shows the dependency of the normalized permeability of the fracture and the whole system on the normalized permeability of the porous matrix for both $h_p/h=10$ and $h_p/h=20$. The value k_c is the permeability calculated by the cubic law with the fracture width, and k_0 is the effective permeability of the whole system under the condition that the porous matrix is impermeable. The value k_p is the permeability of the porous matrix, k_f is the permeability of the fracture, and k_e is the permeability of the whole fractured system. The ratio of k_e to k_0 can be used as an indication of error caused by the cubic law used to calculate the permeability of the whole fractured system. It is clear that when k_p/k_c is less than 10^{-4} k_e/k_0 and k_f/k_c are very close to 1 in both cases. At this small value of k_p/k_c, the permeability of the porous matrix is so small, compared to the fracture, that flow inside it contributes little to the whole system. Hence, the total effective permeability of the fractured system can be calculated as though the porous matrix is impermeable, and the permeability of the fracture can be calculated by the cubic law based on the width of the fracture. As k_p/k_c increases to about 10^{-4}, k_e/k_0 of the case $h_p/h=20$ begins to increase.

With the further increase of k_p/k_c, the k_e/k_0 of the case $h_p/h=10$ also begins to increase. As k_p/k_c exceeds 10^{-3}, k_f/k_c in both cases begins to increase. The dependency curves of k_f/k_c on k_p/k_c in the two geometries coincide with each other. This is reasonable: when h_p is big enough, the flow in the porous matrix away from the fracture becomes uniform; the permeability of the fracture does not depend on h_p. The normalized permeability of the whole system,

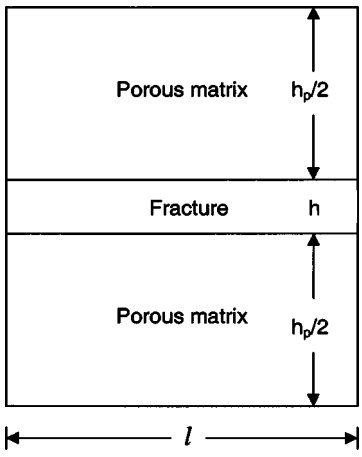

FIG. 9. Geometry of a simplified fractured system.

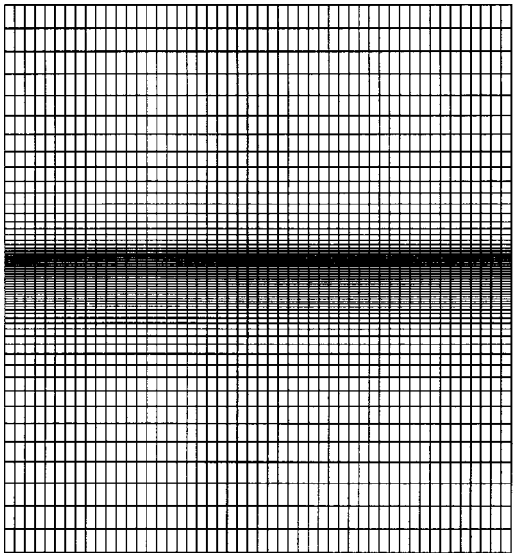

FIG. 10. Nonuniform rectangular mesh used in the simulations of the simplified fractured system with $h_p/h=10$.

k_e/k_0, however, does depend on the width ratio of the porous matrix to the fracture. At a given value of k_p/k_c greater than 10^{-4}, the k_e/k_0 of $h_p/h=20$ is larger than that of $h_p/h=10$. That is, when the width ratio is big enough, although the flow in the porous matrix is still very small, the contribution of the porous matrix to the fractured system is not negligible due to its large size compared to the fracture. The cubic law used in this case to calculate the fracture permeability will incur significant error. This also means that the higher the ratio, the more significant the error caused by using the cubic law, and hence the stricter the conditions of using the cubic law to calculate the fracture permeability.

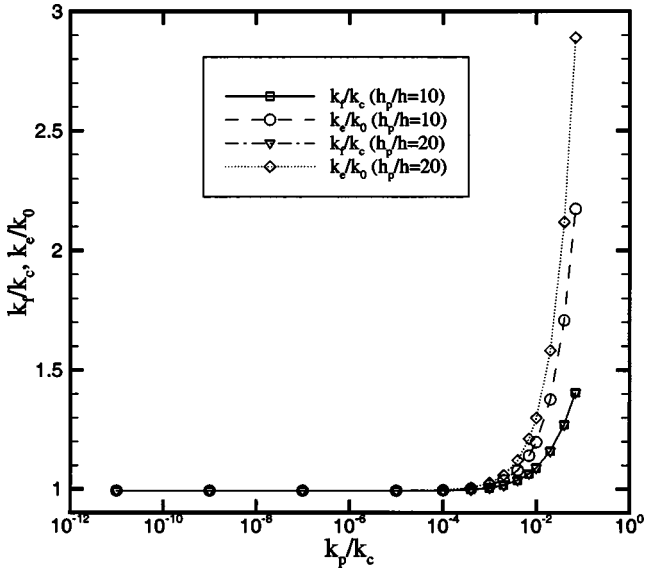

FIG. 11. Dependency of k_f/k_c and k_e/k_0 on k_p/k_c, where k_c is the permeability calculated by the cubic law with the fracture width; k_0 is the effective permeability of the whole system under the condition that the porous matrix is impermeable; k_p is the permeability of the porous matrix; k_f is the permeability of the fracture; and k_e is that of the whole fractured system.

Figure 12 illustrates the horizontal velocity profiles (normalized by the centerline velocity of the fracture) of the flow through the fractured system with $h_p/h=10$ at $k_p/k_c=10^{-5}$, 10^{-2}, and 10^{-1}. At $k_p/k_c=10^{-5}$, the velocity profile in the fracture is parabolic, and the velocity is almost zero in porous matrix. The interface between the porous matrix and the fracture is very sharp. At $k_p/k_c=10^{-2}$ and 10^{-1}, the flux in the porous matrix has a finite value, although small, and makes a significant contribution to the system since the size of the porous matrix is much larger than that of the fracture. Now the interface between the porous matrix and the fracture is smoother, indicating an interaction between the porous matrix and the fracture. As a result, the flux in the porous matrix very close to the interface is larger than that flux far away. Now the velocity profile in the fracture is no longer parabolic because the no-slip boundary condition is not satisfied at the interface. In this situation, a direct use of the cubic law will cause significant error.

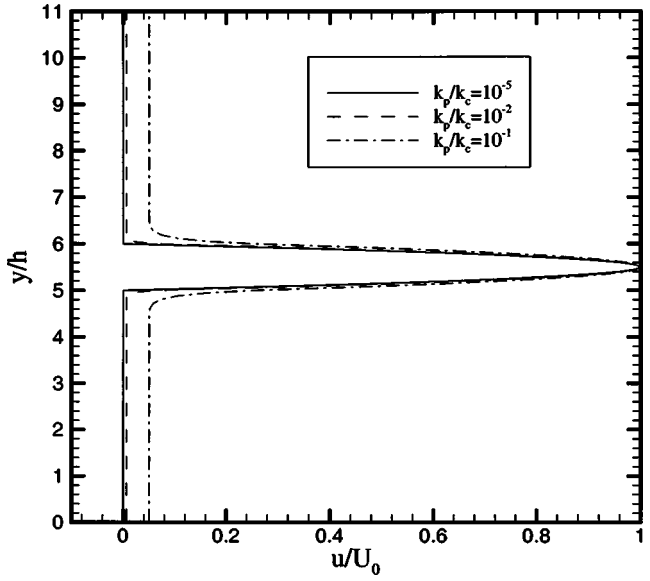

FIG. 12. The horizontal velocity profiles (normalized by the centerline velocity of the fracture) at $k_p/k_c=10^{-5}$, 10^{-2}, and 10^{-1}.

IV. CONCLUSIONS

We have developed a unified microscopic/macroscopic porous media method capable of simulating flow in various-length-scale porous systems and in systems where multiple length scales coexist.

Application of this method to a unidirectional steady flow through a homogeneous and a heterogeneous porous medium recovered Darcy's law when the effects of inertial forces and the Brinkman correction can be neglected. Direct use of this model on the usual computational nodes, with zero resistance on void spaces and infinite resistance on solid walls, gave results that agree very well with the analytical solutions.

Simulations performed on a fractured porous system indicated that, as far as the overall permeability of the system was concerned, the current method gave a very good result, and that the method presented here is capable of handling fractured systems with large length-scale spans.

Simulations were also performed on a simplified fractured system. In the vicinity of the fracture, fine grids are used so the effects of the fracture are counted. Far from the fracture, coarse grids are used, so simulation size can be very large. The dependency of the normalized permeability of the fracture and the whole system on the normalized permeability of the rock matrix was shown. It is clear that, when the ratio of permeability of the porous matrix to that of the fracture calculated by the cubic law is less than 10^{-4}, the effects of the flow in the rock matrix are negligible, and discrete-fracture models that ignore the flow in the matrix are plausible. When the ratio is larger than 10^{-4}, the flow in the matrix has significant effects on the fractured system, and the assumption that the matrix is impermeable does not hold. Therefore, the use of the cubic law to calculate the fracture permeability will cause significant errors. It was also indicated that the threshold value of 10^{-4} is not fixed. As the width ratio of the porous matrix to the fracture increases, the conditions for using the cubic law are stricter.

In this study, we used only rectangular grids in all the meshes, including the nonuniform ones, to validate our method. To simulate flow in realistic porous or fractured media, it is necessary to extend our method to curvilinear coordinate systems or composite grids. This is the topic of our future work.

ACKNOWLEDGMENTS

This study was partially funded by LDRD/ER Project No. 99025 from Los Alamos National Laboratory, which is operated by the University of California for the U.S. Department of Energy. The authors thank Zhiming Lu of Los Alamos National Laboratory for generating the heterogeneous porous medium and providing FEHM simulation results of flow through this medium.

[1] J. Bear, C. F. Tsang, and G. de Marsily, *Flow and Contaminant Transport in Fractured Rock* (Academic, San Diego, CA, 1993).

[2] M. Sahimi, Rev. Mod. Phys. **65**, 1393 (1993).

[3] L. Smith and F. W. Schwartz, in *Flow and Contaminant Transport in Fractured Rock*, edited by J. Bear, C. F. Tsang, and G. de Marsily (Academic, San Diego, CA, 1993), pp. 129–167.

[4] S. H. Lee, M. F. Lough, and C. L. Jensen, Water Resour. Res. **37**, 443 (2001).

[5] J. C. S. Long, P. Gilmour, and P. A. Witherspoon, Water Resour. Res. **21**, 1105 (1985).

[6] W. S. Dershowitz, Ph.D. thesis, Massachusetts Institute of Technology, Cambridge, 1985.

[7] J. Anderson and B. Dverstorp, Water Resour. Res. **23**, 1876

(1987).
[8] M. C. Cacas, E. Ledoux, G. de Marsily, B. Tille, A. Barbreau, E. Durand, B. Feuga, and P. Peaudecerf, Water Resour. Res. **26**, 479 (1990).
[9] P. A. Hsieh and S. P. Neuman, Water Resour. Res. **21**, 1655 (1985).
[10] J. C. S. Long and P. A. Witherespoon, J. Geophys. Res. [Solid Earth Planets] **90**, 3087 (1985).
[11] S. P. Neuman, in *Rock Mechanics: Proceedings of the 28th U.S. Symposium*, edited by I. W. Farmer *et al.* (Balkema, Boston, MA, 1987), pp. 533–561.
[12] B. Berkowitz, J. Bear, and C. Braester, Water Resour. Res. **24**, 1225 (1988).
[13] T. M. Clemo and L. Smith, EOS Trans. Am. Geophys. Union **70**, 1088 (1989).
[14] X. H. Wen, C. S. Kung, and V. Cvetkovic (unpublished).
[15] S. Chen and G. D. Doolen, Annu. Rev. Fluid Mech. **30**, 329 (1998).
[16] R. Benzi, S. Succi, and M. Vergassola, Phys. Rep. **222**, 145 (1992).
[17] D. H. Rothman and S. Zaleski, Rev. Mod. Phys. **66**, 1417 (1994).
[18] S. Chen, S. P. Dawson, G. D. Goolen, D. R. Janecky, and A. Lawniczak, Comput. Chem. Eng. **19**, 617 (1995).
[19] Y. Qian, S. Succi, and S. A. Orszag, Annu. Rev. Comput. Phys. **3**, 195 (1995).
[20] S. Succi, E. Foti, and F. Higuera, Europhys. Lett. **10**, 433 (1989).
[21] A. Cancelliere, C. Chang, E. Foti, D. H. Rothman, and S. Succi, Phys. Fluids A **2**, 2085 (1990).
[22] A. W. J. Heijs and C. P. Lowe, Phys. Rev. E **51**, 4346 (1995).
[23] A. K. Gunstensen and D. H. Rothman, J. Geophys. Res. [Solid Earth] **98**, 6431 (1993).
[24] D. Zhang, R. Zhang, S. Chen, and W. E. Soll, Geophys. Res. Lett. **27**, 1195 (2000).
[25] Q. Kang, D. Zhang, S. Chen, and X. He, Phys. Rev. E **65**, 036 318 (2002).
[26] K. Balasubramanian, F. Hayot, and W. F. Saam, Phys. Rev. A **36**, 2248 (1987).
[27] M. A. A. Spaid and F. R. Phelan, Jr., Phys. Fluids **9**, 2468 (1997).
[28] D. M. Freed, Int. J. Mod. Phys. C **9**, 1491 (1998).
[29] X. He and L. S. Luo, Phys. Rev. E **55**, R6333 (1997).
[30] T. Abe, J. Comput. Phys. **131**, 241 (1997).
[31] F. Nannelli and S. Succi, J. Stat. Phys. **68**, 401 (1992).
[32] S. Succi, G. Amati, and R. Benzi, J. Stat. Phys. **81**, 5 (1995).
[33] H. Xi, G. Peng, and S. H. Chou, Phys. Rev. E **59**, 6202 (1999).
[34] X. He, L. S. Luo, and M. Dembo, J. Comput. Phys. **129**, 357 (1996).
[35] X. He and G. D. Doolen, Phys. Rev. E **56**, 434 (1997).
[36] X. He and G. D. Doolen, J. Comput. Phys. **134**, 306 (1997).
[37] R. Mei and W. Shyy, J. Comput. Phys. **143**, 426 (1998).
[38] O. Filippova and D. Hanel, J. Comput. Phys. **147**, 219 (1998).
[39] R. Mei, L. Luo, and W. Shyy, J. Comput. Phys. **155**, 307 (1999).
[40] R. Mei, W. Shyy, D. Yu, and L. Luo, J. Comput. Phys. **161**, 680 (2000).
[41] C. L. Lin and Y. G. Lai, Phys. Rev. E **62**, 2219 (2000).
[42] T. Lee and C. L. Lin, J. Comput. Phys. **171**, 336 (2001).
[43] X. Shan and H. Chen, Phys. Rev. E **47**, 1815 (1993).
[44] N. S. Martys and H. Chen, Phys. Rev. E **53**, 743 (1996).
[45] H. C. Brinkman, Appl. Sci. Res., Sect. A **1**, 27 (1947).
[46] F. F. Abraham, J. Q. Broughton, N. Bernstein, and E. Kaxiras, Comput. Phys. **12**, 538 (1998).
[47] F. Mazzocco, C. Arrighetti, G. Bella, L. Spagnoli, and S. Succi, Int. J. Mod. Phys. C **11**, 233 (2000).
[48] O. Filippova, S. Succi, F. Mazzocco, C. Arrighetti, G. Bella, and D. Hanel, J. Comput. Phys. **170**, 812 (2001).
[49] S. Succi, O. Filippova, G. Smith, and E. Kaxiras, Comput. Sci. Eng. **3**, 26 (2001).
[50] A. R. Mehrabi and M. Sahimi, Phys. Rev. Lett. **79**, 4385 (1997).
[51] Q. Zou and X. He, Phys. Fluids **9**, 1591 (1997).
[52] C. V. Deutsch and A. G. Journel, *GSLIB: Geostatistical Software Library* (Oxford University Press, New York, 1992).
[53] G. A. Zyvoloski, B. A. Robinson, Z. V. Dash, and L. L. Trease, Los Alamos National Laboratory Report No. LA-13307-MS, 1997 (unpublished).